PHYSICAL REVIEW A **100**, 063630 (2019)

Rashba and Weyl spin-orbit coupling in an optical lattice clock

Xiaofan Zhou,[1,2] Xi-Wang Luo,[1] Gang Chen,[2,3,4,*] Suotang Jia,[2,3] and Chuanwei Zhang[1,†]
[1]*Department of Physics, The University of Texas at Dallas, Richardson, Texas 75080, USA*
[2]*State Key Laboratory of Quantum Optics and Quantum Optics Devices, Institute of Laser spectroscopy, Shanxi University, Taiyuan 030006, China*
[3]*Collaborative Innovation Center of Extreme Optics, Shanxi University, Taiyuan, Shanxi 030006, China*
[4]*Collaborative Innovation Center of Light Manipulations and Applications, Shandong Normal University, Jinan 250358, China*

(Received 9 May 2018; published 17 December 2019)

Recent experimental realization of one-dimensional spin-orbit coupling (SOC) for ultracold alkaline-earth(-like) atoms in optical lattice clocks opens a new avenue for exploring exotic quantum matter because of the strongly suppressed heating of atoms from lasers comparing with alkaline-earth atoms. Here we propose a scheme to realize two-dimensional (2D) Rashba and three-dimensional (3D) Weyl types of SOC in a 3D optical lattice clock and explore their topological phases. With 3D Weyl SOC, the system can support topological phases with various numbers as well as types (I or II) of Weyl points. The spin distributions of such topological bands for 2D Rashba and 3D Weyl SOCs can be detected using suitably designed spectroscopic sequences. Our proposal may pave the way for the experimental realization of robust topological quantum matters and their exotic quasiparticle excitations in ultracold atomic gases.

DOI: 10.1103/PhysRevA.100.063630

I. INTRODUCTION

Spin-orbit coupling (SOC) plays a key role for many condensed-matter phenomena, such as anomalous and spin Hall effects [1], topological insulators and superconductors [2–4], etc. The recent experimental realization of one-dimensional (1D) [5–12] and two-dimensional (2D) [13–15] SOCs in ultracold alkaline-earth atoms provides a highly controllable and disorder-free platform for exploring nontrivial topological physics induced by SOC, such as Majorana fermions with non-Abelian exchange statistics [16–19] and Weyl fermions [20–24] carrying topological monopole charges [25]. The magnetic coupling schemes are also explored to generate 2D SOC [26–28]. However, the experimental observation of these topological phenomena is greatly hindered by the heating of atoms, particularly fermions, originating from the Raman process where lasers couple hyperfine ground states with high-lying excited states. The single-photon detuning for Raman lasers is limited by the fine-structure splitting [5–15,29–31] for the generation of SOC, which is usually small for alkaline-earth atoms, yielding large spontaneous emission of photons that heat the atomic gas.

The heating issue may be overcome by choosing atomic species with large fine-structure splitting such as Dy and Er [32,33] or using alkaline-earth(-like) atoms [34,35] with long-lived excited states [e.g., the lifetime for ^{87}Sr (^{173}Yb) is $\approx$160 ($\approx$20) s [36,37]]. For alkaline-earth(-like) atoms, 1D SOC has been theoretically proposed [35] and experimentally realized [36–38] recently through directly coupling the ground $^1S_0$ (referred to as $|g\rangle$) and excited metastable $^3P_0$ (referred to as $|e\rangle$) clock states in 1D optical lattice clocks, which does not involve any Raman process. With the recent experimental success in realizing 2D and three-dimensional (3D) optical lattice clocks for both Bose and Fermi atoms [39–42], a natural question is whether 2D and 3D SOCs can also be realized without any Raman process.

Here, we address this important question by proposing a scheme for realizing both 2D Rashba and 3D Weyl types of SOC for alkaline-earth(-like) atoms in a 3D optical lattice clock [43] using Rabi process without involving Raman process. The experimental realization of the proposed scheme should pave the way for the eventual experimental generation of stable topological superfluids without heating induced by spontaneous emission and the observation of topological Majorana [18,19] and Weyl fermions [20–22] in ultracold atomic gases. Our main results are as follows.

(i) Beside the 3D optical lattice potential generated with magic wavelength lasers, the folded (bow-tie) geometry beams are used to generate 3D Weyl (2D Rashba) types of SOC (see Fig. 1). Three-dimensional Weyl (2D Rashba) types of SOC are realized when the wave vectors of the clock laser do (not) possess z components. Rashba SOC represents the interaction between the spin and momentum of a particle in two dimensions [28], which can be described by a momentum-dependent Zeeman interaction $\mu B_k \propto \sigma_x k_y - \sigma_y k_x$ [29] . Weyl-type SOC [30] $\propto \sigma_x k_x + \sigma_y k_y + \sigma_z k_z$ represents a Weyl point, which was initially conceived to describe neutrinos in particle physics and has been widely examined in a class of solid-state materials dubbed Weyl semimetals.

(ii) In the presence of 3D Weyl types of SOC, there exists a rich phase diagram containing topological phases with various number of Weyl points as well as a fully gapped 3D Chern insulator phase. The Weyl points can be type I or type

---

[*] chengang971@163.com

[†] chuanwei.zhang@utdallas.edu

©2019 American Physical Society

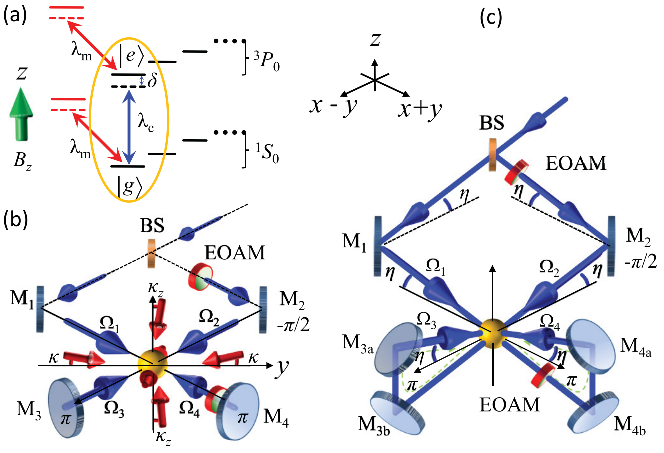

FIG. 1. Schematics of the proposed experimental setup for generating 2D Rashba and 3D Weyl SOCs. (a) Optical transitions. With a magnetic field B applied along the z direction, two nuclear-spin-polarized states can be isolated and chosen as two spin states $|g\rangle$ and $|e\rangle$ for the SOC. The blue arrow represents the clock laser transition, with the single-photon detuning δ. Red arrows represent magic wavelength lasers for 3D optical lattices. (b) Laser setup for 2D Rashba SOC. (c) Clock laser setup for 3D Weyl SOC. Optical lattice lasers are the same as (b). Here EOAM represents an electro-optic amplitude modulator which is used to turn on and off relevant laser beams for the experimental detection.

II [21,44]. Different Weyl points with opposite topological charges are connected by gapless Fermi arcs on the surface.

(iii) A spectroscopic sequence scheme is proposed to accurately measure the spin textures, i.e., the expectation of the spin vector in the momentum space, of the topological bands for 2D Rashba and 3D Weyl SOCs using a combination of Rabi spectroscopy and time-of-flight images.

II. EXPERIMENTAL SCHEME

Our proposed experimental scheme for generating SOC of alkaline-earth(-like) atomic gases ^{87}Sr (^{173}Yb) [35–38] is illustrated in Fig. 1. A large magnetic field is applied along the z direction so that only two nuclear-spin-polarized states ($|g\rangle$ and $|e\rangle$ that form an effective spin-1/2) in ground $^1S_0$ and metastable excited $^3P_0$ manifolds are populated and coupled by a clock laser [see Fig. 1(a)]. The state-independent 3D optical lattice potential $V_{\text{lat}}(\mathbf{r}) = -V_0[\cos^2(k_L x) + \cos^2(k_L y)] - V_z \cos^2(k_L^z z)$ is implemented using six plane-wave lasers [see red arrows in Fig. 1(b)]. The lasers have the magic wavelength λ_m (813 nm for ^{87}Sr and 759 nm for ^{173}Yb) [43], thus $|g\rangle$ and $|e\rangle$ suffer the same lattice potential. Here $k_L = 2\pi \cos(\kappa)/\lambda_m$ and $k_L^z = 2\pi \cos(\kappa_z)/\lambda_m$ are the wave vectors in the x-y plane and z direction, with κ and κ_z corresponding laser incident angles. To avoid interference effects, the magic lasers along different directions are slightly detuned by 10^1 MHz, which would lead to a difference in the lattice potential for the two clock states. The difference is about $10^{-17}V_0$ and can be entirely neglected. Therefore, the two clock states still experience the same lattice potential.

The two states $|g\rangle$ and $|e\rangle$ are coupled by a clock laser with wavelength λ_c (698 nm for ^{87}Sr and 578 nm for ^{173}Yb). In the rotating frame, the single-particle Hamiltonian can be written as

$$H = \left[\frac{\mathbf{p}^2}{2m} + V_{\text{lat}}(\mathbf{r})\right]I + m_z\sigma_z + \hbar(M\sigma_+ + \text{H.c.}), \quad (1)$$

where $\mathbf{p}$ is the momentum operator, m is the mass of atoms, $m_z = \hbar\delta$ is the effective Zeeman field determined by the clock laser detuning, and σ_j (I) is the Pauli (identity) matrix on the $\{|g\rangle, |e\rangle\}$ basis. For the generation of 2D and 3D SOCs, the spatial distribution of the Rabi coupling of the clock laser is designed to be $M = M_0 e^{-ik_R^z z}[\sin(k_c x)\cos(k_c y) + i\cos(k_c x)\sin(k_c y)]$, which can be realized through suitable interference of the clock laser beams.

Figure 1(b) shows the experimental setup for realizing 2D Rashba SOC ($k_R^z = 0$), where the clock laser (linearly polarized along the z direction) is split into two lasers by a beam splitter (BS) and reflected by mirrors M_1, M_2, M_3, and M_4, and propagates along the $(x \pm y)$ directions in the intersecting area with corresponding Rabi frequencies $\Omega_1 = \Omega_0 e^{ik_c(x+y)}$, $\Omega_2 = \Omega_0 e^{ik_c(x-y)+i\varphi_2}$, $\Omega_3 = \Omega_0 e^{-ik_c(x-y)+i(\varphi_2+\varphi_3)}$, and $\Omega_4 = \Omega_0 e^{-ik_c(x+y)+i\varphi_4}$. Here $k_c = 2\pi/(\sqrt{2}\lambda_c)$. Without loss of generality, we set Ω_0 to be real because its overall phase originating from the initial phase of the incident laser can be gauged out without affecting the SOC. φ_2 (φ_3 or φ_4) is the phase acquired by the beam when it propagates along the optical path from the atom cloud over mirrors $M_{1,2}$ (M_3 or M_4) then back to the atom cloud. The total Rabi coupling strength $M = \sum_{\Lambda=1}^{4} \Omega_\Lambda$ has the above-designed form by choosing $\varphi_2 = -\pi/2$, $\varphi_3 = \pi$, $\varphi_4 = \pi$, and $M_0 = 2\sqrt{2}\Omega_0$. We choose $k_c = k_L$ for the generation of desired 2D Rashba SOC, yielding $\cos(\kappa) = \lambda_m/(\sqrt{2}\lambda_c) \approx 0.8$ for ^{87}Sr (0.9 for ^{173}Yb).

The generation of 3D SOC requires the phase factor $e^{-ik_R^z z}$ in the Rabi coupling M, which can be realized by tilting the four clock laser beams Ω_Λ by an angle η with respect to the $x - y$ plane with $k_R^z = 2\pi\sin(\eta)/\lambda_c$. In the x-y plane, $k_L = k_c = 2\pi\cos(\eta)/(\sqrt{2}\lambda_c)$ yields $\cos(\kappa)/\cos(\eta) = \lambda_m/(\sqrt{2}\lambda_c)$. Such 3D Ω_Λ can be realized with a similar optical setup with mirrors and a beam splitter [see Fig. 1(c)]. Note that the electric field of the clock laser has a component in the x-y plane, which, however, does not induce the transition to other nuclear-spin states due to the large Zeeman splitting [see Fig. 1(a)]. Such direct Rabi coupling between two pseudospin states using clock lasers for alkaline-earth atoms does not involve the two-photon Raman transition process that was used for alkaline-earth atoms. In the two-photon Raman process, lasers couple hyperfine ground states with high-lying excited states, which induce large spontaneous emission of photons. Furthermore, the Raman transition between different Zeeman states requires careful design of laser polarizations of Raman beams, which is not necessary for the Rabi transition here. Note that the gravity of the Earth has to be considered for the 3D geometry. The gravity would tilt the lattice by introducing a neighboring-site (z-direction) detuning ≈1 kHz [45–48] which may lead to Bloch oscillations and Wannier-Stark states, and the system ends up in the continuum in the long-time limit because there are no true bound states. To avoid such gravity effect, one might apply a gradient ac-Stark shift [49,50]. Alternatively, one can introduce additional harmonic traps to confine the atoms (usually the case in realistic experiments), where the gravity potential only shifts the minimum of the harmonic traps [51,52].

III. THEORETICAL MODELING

With typical optical lattice potential depths, atoms are confined in the lowest band of the lattice and tight-binding approximation can be applied. After the single-band approximation and the unitary transformation $U = e^{-ik_{\rm R}^z z/2}|g\rangle\langle g| + e^{ik_{\rm R}^z z/2}|e\rangle\langle e|$, we obtain the tight-binding Hamiltonian from Eq. (1), which can be written as

$$\begin{aligned}\mathcal{H}_{\rm TI} = {}& -t\sum_{\langle\vec{j},\vec{j}'\rangle}\hat{c}^\dagger_{\vec{j}s}\hat{c}_{\vec{j}'s} + m_z\sum_{\vec{j}}(\hat{n}_{\vec{j}g}-\hat{n}_{\vec{j}e}) \\ & + \sum_{\langle\vec{j},\vec{j}'\rangle}\big[t_{\rm SO}^{\vec{j},\vec{j}'}\hat{c}^\dagger_{\vec{j}g}\hat{c}_{\vec{j}'e}+\text{H.c.}\big] \\ & - t_z\sum_{j_z}(e^{i\phi\xi_s/2}\hat{c}^\dagger_{j_zs}\hat{c}_{j_z+1s}+\text{H.c.}),\end{aligned} \qquad (2)$$

where $\langle\ \rangle$ denotes the sum over nearest-neighbor sites with x-y plane lattice-site index $\vec{j} = (j_x, j_y)$, particle number operators $\hat{n}_{\vec{j}s} = \hat{c}^\dagger_{\vec{j}s}\hat{c}_{\vec{j}s}$, and effective Zeeman field $m_z = \hbar\delta$. t is the spin-preserved hopping amplitude along the x (y) direction, and $t_{\rm SO}^{\vec{j},\vec{j}'} = \int d^2rW_g(r-r_j)MW_e(r-r_{j'})$ is the spin-flipped hopping parameter along the x (y) direction with $W_{g,e}(r-r_j)$ the Wannier function at site j. Notice that the spatial period of M (in both x and y directions) is twice that of the period of the optical lattice. As a result, we have $t_{\rm SO}^{\vec{j},\vec{j}\pm\vec{e}_\mu} = \pm(-1)^{j_x+j_y}t^\mu_{\rm SO}$, with $\mu = x, y$. For the aforementioned clock transition M, we have $t^x_{\rm SO} = -it^y_{\rm SO} = t_{\rm SO}$. $t_{\rm SO}$ can be tuned by changing the amplitude of the clock laser's Rabi coupling Ω_0. The last term in Eq. (2) corresponds to spin conserved hopping along the z direction, where t_z is the hopping amplitude, $\phi = \pi k^z_{\rm R}/k^z_{\rm L}$ is the hopping phase (it can be tuned by the angle between the plane-wave laser pair that forms the z-direction lattice), and $\xi_{g,e} = \pm 1$. Due to the spatial dependence of the SOC, the Hamiltonian on the xy plane has a period $2a$, which can be restored to a by applying the unitary transformation $\hat{c}_{\vec{j}e} \longrightarrow e^{i\pi(x_j+y_j)/a}\hat{c}_{\vec{j}e}$ with a the optical lattice constants in the x-y plane. With the lattice translational symmetry, the momentum is a good quantum number and the single-particle Hamiltonian can be exactly diagonalized in the momentum space. Physical results such as energy spectrum, topological charge of the Weyl point, and phase boundary can be calculated analytically. Fourier transformation of the real-space Hamiltonian to the momentum space yields the effective Hamiltonian

$$\mathcal{H}_{\rm E} = \sum_{\mathbf{k},ss'}\hat{c}^\dagger_{\mathbf{k},s}\mathbf{H}_\mathbf{k}\hat{c}_{\mathbf{k},s'}, \qquad (3)$$

where $s = (g, e)$, and $\hat{c}^\dagger_{\mathbf{k},s}$ ($\hat{c}_{\mathbf{k},s}$) is the creation (annihilation) operator for state s at momentum $\mathbf{k} = (k_x, k_y, k_z)$. $\mathbf{H}_\mathbf{k} = h_{0\mathbf{k}}I + \mathbf{h}_\mathbf{k}\cdot\sigma$, where $h_{0\mathbf{k}} = -2t_z\cos(k_za_z)\cos(\phi/2)$, $h_{x\mathbf{k}} = -2t_{\rm SO}\sin(k_ya)$, $h_{y\mathbf{k}} = -2t_{\rm SO}\sin(k_xa)$, and $h_{z\mathbf{k}} = m_z - 2t\cos(k_xa) - 2t\cos(k_ya) + 2t_z\sin(k_za_z)\sin(\phi/2)$. a_z are the optical lattice constants in the z direction. The energy spectrum of the Hamiltonian can be easily obtained through diagonalizing the $\mathbf{H}_\mathbf{k}$, yielding $E_\mathbf{k} = h_{0\mathbf{k}} \pm |\mathbf{h}_\mathbf{k}|$.

When $k^z_{\rm R} = 0$ (i.e., the clock laser is in the x-y plane), $\phi = 0$ and $h_{z\mathbf{k}} = m_z - 2t\cos(k_xa) - 2t\cos(k_ya)$, therefore there is no coupling between momentum k_z and spin, leaving 2D Rashba-type SOC in the x-y plane in the Hamiltonian Eq. (3). In this case, the single-particle physics is described by a topological phase transition between a trivial insulator for $|m_z| > 4t$ and a topological insulator for $|m_z| < 4t$, with the phase boundary $|m_z| = 4t$ determined by $|\mathbf{h}_\mathbf{k}| = 0$ [14,53]. Such 2D Rashba SOC not only mixes states $|g\rangle$ and $|e\rangle$, but also lifts the band degeneracy with a single Fermi surface. In the presence of s-wave pairing interaction between two states, the fermionic superfluid pairing supports Majorana fermions inside vortex cores [18,19], which possess non-Abelian exchange statistics and are a building block for fault-tolerant topological quantum computation [16,17].

IV. TOPOLOGICAL PHASES WITH 3D SOC

When $k^z_{\rm R} \neq 0$, $\phi = \pi k^z_{\rm R}/k^z_{\rm L} \neq 0$, and the Hamiltonian Eq. (3) contains the coupling $2t_z\sin(k_za_z)\sin(\phi/2)\sigma_z$ along the k_z direction, leaving 3D Weyl SOC. We first consider $\phi = \pi$ (i.e., $k^z_{\rm R} = k^z_{\rm L}$), which leads to $h_{0\mathbf{k}} = 0$. From the energy dispersion $E_\mathbf{k} = \pm|\mathbf{h}_\mathbf{k}|$, we see the spectrum is gapless only when $|\mathbf{h}_\mathbf{k}| = 0$, with $h_{x\mathbf{k}} = h_{y\mathbf{k}} = 0$ occurring at $k_xa, k_ya = 0$ or π. Each band-gap closing point with $E_\mathbf{k} = 0$ represents a Weyl point [see Fig. 2(a)], the topological charge of which can be determined by Chern number $\mathcal{C} = \frac{1}{2\pi}\oint_S B(\mathbf{k})dS$ of the lowest energy band. Here S is a surface enclosing the

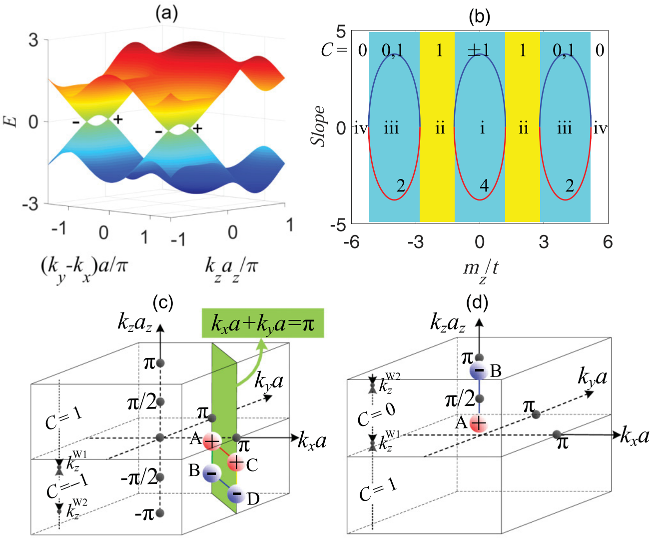

FIG. 2. Topological phases in three dimensions with $\phi = \pi$. In all panels $t_{\rm SO}/t = 0.6$, $t_z/t = 0.6$. (a) Energy spectrum $E_\mathbf{k}$ with four Weyl points in the $k_xa + k_ya = \pi$ plane, with their topological charges ± 1. $m_z/t = 1$. (b) The phase diagram with different m_z. (2,4,2) indicates the number of Weyl points. Blue and red lines represent two slopes $\pm 2t_z\cos(\gamma)$ of the energy dispersions along the k_z direction near a Weyl point. The Chern number C is defined in the $k_x - k_y$ plane for fixed k_za_z. (c, d) Positions and charges of Weyl points as well as the Chern numbers for cases i and iii, respectively.

Weyl point, and $B(\mathbf{k}) = i\langle\nabla_{\mathbf{k}}\Psi(\mathbf{k})| \times |\nabla_{\mathbf{k}}\Psi(\mathbf{k})\rangle$ is the Berry curvature [1] with $\Psi(\mathbf{k})$ the lower band wave function.

For $t_z < t$, at $(k_x a, k_y a) = (0, \pi)$ or $(\pi, 0)$, $h_{z\mathbf{k}} = m_z + 2t_z \sin(k_z a_z)$ becomes zero in the region $|m_z| \leqslant 2t_z$ at $k_z a_z = \gamma$ or $-\pi - \gamma$ with $\gamma = \arcsin[\frac{-m_z}{2t_z}]$, while, at $(k_x a, k_y a) = (0, 0)$ or (π, π), $h_{z\mathbf{k}} = m_z \mp 4t + 2t_z \sin(k_z a_z)$ becomes zero only in the region $4t - 2t_z \leqslant \pm m_z \leqslant 4t + 2t_z$ at $k_z a_z = \zeta$ or $\pi - \zeta$ with $\zeta = \arcsin[\frac{\pm 4t - m_z}{2t_z}]$, where the top and bottom signs are for $(0, 0)$ and (π, π), respectively. Outside these two regions ($2t_z < |m_z| < 4t - 2t_z$ and $|m_z| > 4t + 2t_z$), the spectrum is fully gapped. Based on the above gap closing conditions, there exist four different phases in different m_z regions [see Fig. 2(b)].

(i) When $|m_z| \leqslant 2t_z$, we have four Weyl points at $\mathbf{k}^W = (k_x a, k_y a, k_z a_z) = (0, \pi, \gamma)$, $(0, \pi, -\pi - \gamma)$, $(\pi, 0, \gamma)$, and $(\pi, 0, -\pi - \gamma)$ with different topological charges ± 1 [see Fig. 2(c)]. The Chern number in the k_x-k_y plane changes ± 2, when the varying $k_z a_z$ crosses the two Weyl points (A, C) with topological charge $+1$ at k_z^{W1}. For instance, around $\mathbf{k}^W = (0, \pi, \gamma)$, $\mathbf{h}_{\mathbf{k}} \approx 2t_{\mathrm{SO}} a(\bar{k}_y \sigma_x - \bar{k}_x \sigma_y) + 2t_z a_z \cos(\gamma) \bar{k}_z \sigma_z$ with the linear dispersion, where $\bar{\mathbf{k}} = \mathbf{k} - \mathbf{k}^W$. The energy dispersions along the k_z direction near a Weyl point represent two slopes $\pm 2t_z \cos(\gamma)$ [see Fig. 2(b)]. The two slopes $\pm 2t_z \cos(\gamma)$ have opposite signs, with the corresponding Weyl point type I.

(ii) When $2t_z < |m_z| < 4t - 2t_z$, we have a fully gapped topological phase with Chern number $C = 1$ in the k_x-k_y plane for any fixed k_z, corresponding to a stacking 2D Chern insulator.

(iii) When $4t - 2t_z \leqslant \pm m_z \leqslant 4t + 2t_z$, we have two Weyl points at $\mathbf{k}^W = (0, 0, \zeta)$ and $(0, 0, \pi - \zeta)$ for $m_z > 0$ [see Fig. 2(d)] or (π, π, ζ) and $(\pi, \pi, \pi - \zeta)$ for $m_z < 0$. When $k_z a_z$ crosses one Weyl point (A) with topological charge $+1$ at k_z^{W1}, the Chern number in the k_x-k_y plane changes ± 1. Two slopes $\pm 2t_z \cos(\gamma)$ have opposite signs, corresponding to the type-I Weyl point [see Fig. 2(b)].

(iv) When $|m_z| > 4t + 2t_z$, we have a trivial insulator phase.

For $t_z > t$, there are two cases that are different from $t_z < t$.

(i) When $t < t_z \leqslant 2t$, we have six Weyl points. The region $|m_z| \leqslant 2t_z$ [middle cycle of Fig. 2(b)] overlaps with regions $4t - 2t_z \leqslant m_z < 4t + 2t_z$ [right cycle of Fig. 2(b)] and $-4t - 2t_z < m_z \leqslant -4t + 2t_z$ [left cycle of Fig. 2(b)], leading to six Weyl points in the regions $4t - 2t_z \leqslant m_z \leqslant 2t_z$ and $-2t_z \leqslant m_z \leqslant 2t_z - 4t$.

(ii) When $t_z > 2t$, we have eight Weyl points. All three regions above overlap near $m_z = 0$, leading to a new region $4t - 2t_z \leqslant m_z \leqslant 2t_z - 4t$ with eight Weyl points.

For a general $\phi \neq \pi$, there is a nonzero $h_{0\mathbf{k}} = -2t_z \cos(k_z a_z) \cos(\phi/2)$ and t_z in $h_{z\mathbf{k}}$ is also replaced by $t_z \sin(\phi/2)$. $h_{0\mathbf{k}}$ does not change the eigenstates of the Hamiltonian Eq. (3), therefore the phase boundaries between the above four cases are only changed by the replacement $t_z \to t_z \sin(\phi/2)$. However, nonzero $h_{0\mathbf{k}}$ rotates the slopes of the linear dispersions near the Weyl point such that two slopes along the k_z direction may have the same sign in certain parameter regions, which correspond to type-II Weyl points (the traditional one with opposite signs of slopes is called type I). For instance, around the Weyl point $\mathbf{k}^W = (0, \pi, \gamma)$ for case i $|m_z| \leqslant 2t_z \sin(\phi/2)$, the Hamiltonian can be expanded as $\mathbf{h}_{\mathbf{k}} = v_0 \bar{k}_z + 2t_{\mathrm{SO}} a(\bar{k}_y \sigma_x - \bar{k}_x \sigma_y) + v_z \bar{k}_z \sigma_z$ with $v_0 = 2t_z a_z \sin(\gamma) \cos(\phi/2)$, $v_z = 2t_z a_z \cos(\gamma) \sin(\phi/2)$, and $\gamma = \arcsin[\frac{-m_z}{2t_z \sin(\phi/2)}]$. The Lifshitz transition [54] between type I and type II occurs at $|v_0| = |v_z|$ [i.e., $|m_z^c| = 2t_z \sin^2(\phi/2)$]. The phase diagram and corresponding types of Weyl points are shown in Fig. 3(a).

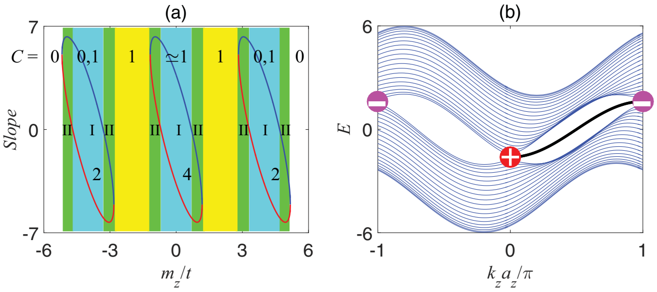

FIG. 3. Type-I and type-II Weyl points for $\phi \neq \pi$. (a) Phase diagram. The notations and parameters are the same as those in Fig. 2(b) except $\phi = 2\pi/5$. Regions I (blue shaded region) and II (green shaded region) indicate the types of the Weyl points. Two slopes are $v_0 \pm v_z$. (b) Energy spectrum $E_{\mathbf{k}}$ under open boundary condition along the x direction with $\phi = 2\pi/5$ and $m_z/t = 0.0$. The black line represents the surface state connecting two Weyl points.

The bulk topological Weyl points yield interesting surface states [55] under open boundary conditions. The Fermi arc is a curve in the energy spectrum on the surface Brillouin zone that connects Weyl points with opposite charges. Because Weyl points do not stay at the $E_{\mathbf{k}} = 0$ plane due to nonzero $h_{0\mathbf{k}}$, the surface states are now embedded in the bulk spectrum [see Fig. 3(b)], instead of the straight Fermi arc at $E_{\mathbf{k}} = 0$ connecting two Weyl points with opposite charges for $\phi = \pi$.

V. EXPERIMENTAL MEASUREMENT OF SPIN TEXTURES

The topological properties of 2D Rashba and 3D Weyl SOC can be characterized by their spin textures in the momentum space, which are shown in Figs. 4(a) and 4(b). The spin texture $\mathbf{S}(\mathbf{k})$ is the expectation value of the Pauli matrix σ

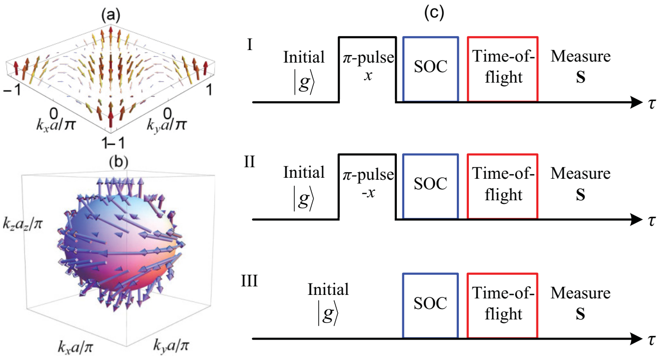

FIG. 4. Detection of spin textures. (a) Spin textures in the k_x-k_y plane with 2D Rashba SOC. $t_{\mathrm{SO}}/t = 0.6$, $m_z/t = 0$. (b) Spin textures around a Weyl point with $+1$ topological charge. $t_{\mathrm{SO}}/t = 0.6$, $t_z/t = 0.6$, $m_z/t = 0$, and $\phi = \pi$. (c) Three spectroscopic sequences I, II, and III for the detection of spin parameters $\theta_{\mathbf{k}}$ and $\varphi_{\mathbf{k}}$.

under the pseudospin $|g\rangle$ and $|e\rangle$ basis, and can be defined as $\langle \mathbf{S}(\mathbf{k})\rangle = \langle c^{\dagger}_{\mathbf{k}s}\sigma_{ss'}c_{\mathbf{k}s'}\rangle/2$. These spin textures are determined by the effective field $\mathbf{h}_{\mathbf{k}}$ in the Hamiltonian Eq. (3) and can be parametrized by angles $\theta_{\mathbf{k}} = \arctan\left(\sqrt{h^2_{x\mathbf{k}} + h^2_{y\mathbf{k}}}/h_{z\mathbf{k}}\right)$ and $\varphi_{\mathbf{k}} = \arctan\left(h_{y\mathbf{k}}/h_{x\mathbf{k}}\right)$ at each momentum $\mathbf{k}$. Here we propose a spectroscopic procedure to determine the parameter $(\theta_{\mathbf{k}}, \varphi_{\mathbf{k}})$ by measuring the time dynamics of spin textures $\langle \mathbf{S}(\mathbf{k})\rangle$, which are obtained through a combination of momentum-resolved Rabi spectroscopy [35] and time-of-flight imaging (see the Appendix). The spectroscopic sequences, as shown in Fig. 4(c), are used to eliminate various side effects and obtain accurate results. In all sequences, atoms are initially prepared in state $|g\rangle$ at half filling without SOC.

(I) First a π pulse along σ_x is applied using the clock laser, which excites atoms from $|g\rangle$ to $|e\rangle$ with a momentum transfer $\mathbf{Q} = (k_c, k_c, k^z_{\mathrm{R}})$ that is the same as that of the SOC. Therefore the π pulse couples two pseudospin states with the same quasimomentum $|g, \mathbf{k}\rangle \leftrightarrow |e, \mathbf{k}\rangle$. Such a π pulse can be implemented using one of the four SOC beams, with the other three turned off by electro-optic amplitude modulators [56], as shown in Figs. 1(b) and 1(c). In the quasimomentum space, the tight-binding dispersion of state $|e\rangle$ is inverted with respect to state $|g\rangle$, therefore the energy splittings at different $\mathbf{k}$ are different. With suitably chosen clock laser frequency, we can selectively excite atoms at certain $\mathbf{k}^*$ using a weak pulse (comparing to the tight-binding bandwidth), such that only atoms near $\mathbf{k}^*$ are excited and atoms away from $\mathbf{k}^*$ are off resonance and remain in state $|g\rangle$. For the ^{87}Sr system, one could use a typical lattice with lattice depth $V_0 \sim 4E_R$ (E_R denotes the single-photon recoil energy) such that the tunneling rate t can be up to a few 10^2 Hz ($\sim 0.1E_R$), which leads to a bandwidth of the order of 1 kHz. Therefore tens-of-Hertz resolution would be enough, and the corresponding pulse duration is about tens of milliseconds. Notice that the resonance momentum $\mathbf{k}^*$ is not single valued, which forms a circle in two dimensions and a surface (spherical for type-I or ellipsoidlike for type-II Weyl points) in three dimensions. We can select a different $\mathbf{k}^*$ by slightly changing the frequency of the π pulse, thus covering the whole momentum space.

After the π pulse, we turn on the 2D (3D) SOC and the system evolves under the Hamiltonian Eq. (3) for an interval τ. Then the SOC and lattice potentials are turned off and the time-of-flight images are taken to determine the spin polarization $\langle \mathbf{S}(\mathbf{k})\rangle$ at each $\mathbf{k}$ on the $\mathbf{k}^*$ ring or surface as a function of τ. Our proposed detection scheme usually separately detects the occupations of two states $|e\rangle$ and $|g\rangle$, which give the z component of the pseudospin. Suitable spin rotations using pulses along different spin axes with clock lasers may be needed before the time of flight to measure different components of $\langle \mathbf{S}(\mathbf{k})\rangle$. For example, in order to detect the x component of the pseudospin, a $\pi/2$ pulse is applied, which transfers the wave function $|\Psi\rangle$ to $|\Psi'\rangle$ with $|\Psi'\rangle = U|\Psi\rangle$ and $U = \exp(i\pi/4\sigma^x)$. The final detection $\langle\Psi|S^x|\Psi\rangle$ becomes $\langle\Psi'|S^z|\Psi'\rangle = \langle\Psi|U^{\dagger}S^zU|\Psi\rangle$. The detection of the y component of the pseudospin is the same as the x component, except $U = \exp(i\pi/4\sigma^y)$.

(II) Sequence II is the same as I except that the π pulse is along $-\sigma_x$, which is used to eliminate effects caused by atoms near resonance momenta $\mathbf{k}^*$ that may be partially pumped to $|e\rangle$ (with amplitude $f_{\mathbf{k}}$). Because of the partial excitation amplitude $f_{\mathbf{k}}$, the spin polarizations $\langle \mathbf{S}(\mathbf{k})\rangle_{\mathrm{I,II}}$ obtained from sequences I or II become complicated functionals of $f_{\mathbf{k}}, \theta_{\mathbf{k}}, \varphi_{\mathbf{k}}$, and τ. However, $f_{\mathbf{k}}$ appears as a simple overall factor in their average (see the Appendix):

$$\frac{\langle \mathbf{S}(\mathbf{k})\rangle_{\mathrm{I}} + \langle \mathbf{S}(\mathbf{k})\rangle_{\mathrm{II}}}{2} = \left(\frac{1}{2} - |f_{\mathbf{k}}|^2\right)\mathbf{T}(\theta_{\mathbf{k}}, \varphi_{\mathbf{k}}, \tau), \tag{4}$$

with $\mathbf{T}(\theta_{\mathbf{k}}, \varphi_{\mathbf{k}}, \tau)$ a simple dynamical function which can be used to determine $\theta_{\mathbf{k}}, \varphi_{\mathbf{k}}$.

(III) Sequence III is the same as I without the π pulse, which is used to filter the dynamics of the excited atoms from the remaining $|g\rangle$ atoms by canceling the 1/2 in Eq. (4). As a result, signals for atoms with momenta far away from $\mathbf{k}^*$ are eliminated because $f_{\mathbf{k}}$ is nonzero only in a narrow interval around the $\mathbf{k}^*$ ring or surface. This process isolates the dynamics of atoms near $\mathbf{k}^*$, and we can then replace $\theta_{\mathbf{k}}, \varphi_{\mathbf{k}}$ by $\theta_{\mathbf{k}^*}, \varphi_{\mathbf{k}^*}$ in Eq. (4), from which we can extract their values (see the Appendix).

VI. DISCUSSIONS AND CONCLUSIONS

Our proposed scheme requires high accuracy control for phases and alignments of coupling and lattice laser beams. The relative phase between Ω_1 and Ω_2 is $\varphi_2 = -\frac{\pi}{2}$ and a small deviation in φ_2 would slightly change the relative phase of the spin-flip tunnelings between neighboring sites t_{SO}, which only slightly modifies the form of SOC and does not affect the topological physics. On the other hand, the relative phase between Ω_2 and Ω_3 (Ω_1 and Ω_4) is $\varphi_3 = \pi$ ($\varphi_4 = \pi$), and a deviation in φ_3 or φ_4 would induce a small displacement of the coupling potential M with respect to the optical lattice. Such a displacement would induce on-site spin flips, yielding an additional Zeeman field along σ_x. When the Zeeman field is too large, the bands become topologically trivial, although the spin-orbit coupling still exists. The Zeeman field is proportional to the on-site integral of the Wannier function, thus a small phase deviation may lead to a sizable Zeeman field comparing to the neighbor-site tunneling t_{SO}. Using Wannier functions of a typical trap depth with $V_0 \sim 4E_R$, we find the error in phase φ_3 and φ_3 should be $\leqslant 3 \times 10^{-2}\pi$ to ensure a Zeeman field smaller than t_{SO}, so that the topological phases survive. Such an error upper bound corresponds to a relative displacement of 15 nm between the coupling and lattice laser potential minima. Using active phase locking, the relative displacement $\lesssim 2$ nm has been demonstrated experimentally for 2D Kagome lattices formed by two different wavelength lasers [57–59]. Such active phase locking can be applied to the lattices formed by clock and magic wavelength lasers. Moreover, the periods of the coupling and lattice potentials should be aligned with high accuracy, which are determined by the incident angles of the beams. Such incident angles can be controlled with 10^{-4} accuracy [57–59], which allows the total displacement over $\approx$100 lattice sites (enough for observing topological physics) to be $\approx$5 nm, which is much smaller than the upper bound 15 nm required for topological phases.

In summary, we proposed a scheme for realizing and detecting 2D Rashba and 3D Weyl types of SOC for alkaline-earth(-like) atoms in optical lattice clocks without involving two-photon Raman process, therefore the heating of atoms due to lasers is strongly suppressed. In combination with s-wave scattering interaction between atoms, our scheme provides a powerful platform for realizing stable topological superfluids and observing associated topological excitations, such as Majorana fermions, which may have potential applications in fault-tolerant topological quantum computation.

ACKNOWLEDGMENTS

X.Z., G.C., and S.J. are supported by National Key Research and Development Program of China under Grant No. 2017YFA0304203, the National Natural Science Foundation of China under Grants No. 11804204, No. 11674200, and No. 1331KSC. X.L. and C.Z. are supported by Air Force Office of Scientific Research Grant No. FA9550-16-1-0387, National Science Foundation Grant No. PHY-1806227, and Army Research Office Grant No. W911NF-17x-1-0128.

APPENDIX: EXPERIMENTAL MEASUREMENT OF SPIN TEXTURES

Before introducing the details of our detection scheme, we first show how the spin polarization evolves under the SOC Hamiltonian. Consider an atom in an arbitrary initial state $|\psi_0(\mathbf{k})\rangle = \alpha|g_{\mathbf{k}}\rangle + \beta|e_{\mathbf{k}}\rangle$ with momentum $\mathbf{k}$. Under the SOC Hamiltonian, the state becomes

$$\begin{aligned}
|\psi_\tau(\mathbf{k})\rangle = {} & \bigg[\left(\alpha\frac{\cos\theta_{\mathbf{k}}+1}{2} + \beta\frac{\sin\theta_{\mathbf{k}}}{2}e^{-i\varphi_{\mathbf{k}}}\right)e^{-iE_{\mathbf{k},-}\tau} \\
& + \left(\alpha\frac{1-\cos\theta_{\mathbf{k}}}{2} - \beta\frac{\sin\theta_{\mathbf{k}}}{2}e^{-i\varphi_{\mathbf{k}}}\right)e^{-iE_{\mathbf{k},+}\tau}\bigg]|g_{\mathbf{k}}\rangle \\
& + \bigg[\left(\alpha\frac{\sin\theta_{\mathbf{k}}}{2}e^{i\varphi_{\mathbf{k}}} + \beta\frac{1-\cos\theta_{\mathbf{k}}}{2}\right)e^{-iE_{\mathbf{k},-}\tau} \\
& - \left(\alpha\frac{\sin\theta_{\mathbf{k}}}{2}e^{i\varphi_{\mathbf{k}}} - \beta\frac{\cos\theta_{\mathbf{k}}+1}{2}\right)e^{-iE_{\mathbf{k},+}\tau}\bigg]|e_{\mathbf{k}}\rangle,
\end{aligned} \tag{A1}$$

after time τ with $E_{\mathbf{k},\pm} = h_{0\mathbf{k}} \pm |\mathbf{h}_{\mathbf{k}}|$.

Due to the Rabi oscillation, the time dynamics of all components' spin polarizations can be characterized as

$$\begin{aligned}
\langle S_z\rangle &= P_z(\alpha,\beta,\tau,\mathbf{k}) \\
&= \tfrac{1}{2}(|\alpha|^2-|\beta|^2)[\cos^2\theta_{\mathbf{k}} + \sin^2\theta_{\mathbf{k}}\cos(2|\mathbf{h}_{\mathbf{k}}|\tau)] \\
&\quad + \tfrac{1}{2}(\alpha\beta^* + \alpha^*\beta)\cos\theta_{\mathbf{k}}\sin\theta_{\mathbf{k}}\cos\varphi_{\mathbf{k}}[1-\cos(2|\mathbf{h}_{\mathbf{k}}|\tau)] \\
&\quad + (-i)\tfrac{1}{2}(\alpha\beta^* - \alpha^*\beta)\sin\theta_{\mathbf{k}}\cos\varphi_{\mathbf{k}}\sin(2|\mathbf{h}_{\mathbf{k}}|\tau),
\end{aligned} \tag{A2}$$

$$\begin{aligned}
\langle S_y\rangle &= P_y(\alpha,\beta,\tau,\mathbf{k}) \\
&= \tfrac{1}{4}(-i)(\alpha^*\beta - \alpha\beta^*)[\sin^2\theta_{\mathbf{k}} + \cos^2\theta_{\mathbf{k}}\cos(2|\mathbf{h}_{\mathbf{k}}|\tau)] \\
&\quad + \tfrac{1}{2}(|\alpha|^2-|\beta|^2)\cos\theta_{\mathbf{k}}\sin\theta_{\mathbf{k}}\sin\varphi_{\mathbf{k}}[1-\cos(2|\mathbf{h}_{\mathbf{k}}|\tau)] \\
&\quad + \tfrac{1}{4}(-i)(\alpha\beta^* - \alpha^*\beta)\sin^2\theta_{\mathbf{k}}\cos 2\varphi_{\mathbf{k}}[1-\cos(2|\mathbf{h}_{\mathbf{k}}|\tau)] \\
&\quad + \tfrac{1}{4}(\alpha\beta^* + \alpha^*\beta)\sin^2\theta_{\mathbf{k}}\sin 2\varphi_{\mathbf{k}}[1-\cos(2|\mathbf{h}_{\mathbf{k}}|\tau)] \\
&\quad + \tfrac{1}{4}(-i)\alpha^*\beta\cos(2|\mathbf{h}_{\mathbf{k}}|\tau) \\
&\quad + \tfrac{1}{4}[2(|\alpha|^2-|\beta|^2)\sin\theta_{\mathbf{k}}\cos\varphi_{\mathbf{k}} \\
&\quad - 2(\alpha^*\beta + \alpha\beta^*)\cos\theta_{\mathbf{k}} - \alpha\beta^*]\sin(2|\mathbf{h}_{\mathbf{k}}|\tau),
\end{aligned} \tag{A3}$$

and

$$\begin{aligned}
\langle S_x\rangle &= P_x(\alpha,\beta,\tau,\mathbf{k}) \\
&= \tfrac{1}{4}(\alpha^*\beta + \alpha\beta^*)[\sin^2\theta_{\mathbf{k}} + \cos^2\theta_{\mathbf{k}}\cos(2|\mathbf{h}_{\mathbf{k}}|\tau)] \\
&\quad + \tfrac{1}{2}(|\alpha|^2-|\beta|^2)\cos\theta_{\mathbf{k}}\sin\theta_{\mathbf{k}}\cos\varphi_{\mathbf{k}}[1-\cos(2|\mathbf{h}_{\mathbf{k}}|\tau)] \\
&\quad + \tfrac{1}{4}(\alpha\beta^* + \alpha^*\beta)\sin^2\theta_{\mathbf{k}}\cos 2\varphi_{\mathbf{k}}[1-\cos(2|\mathbf{h}_{\mathbf{k}}|\tau)] \\
&\quad + \tfrac{1}{4}i(\alpha\beta^* - \alpha^*\beta)\sin^2\theta_{\mathbf{k}}\sin 2\varphi_{\mathbf{k}}[1-\cos(2|\mathbf{h}_{\mathbf{k}}|\tau)] \\
&\quad + \tfrac{1}{4}\alpha^*\beta\cos(2|\mathbf{h}_{\mathbf{k}}|\tau) \\
&\quad + \tfrac{1}{4}[2(|\alpha|^2-|\beta|^2)\sin\theta_{\mathbf{k}}i\sin\varphi_{\mathbf{k}} \\
&\quad - 2(\alpha^*\beta - \alpha\beta^*)\cos\theta_{\mathbf{k}} + \alpha\beta^*]i\sin(2|\mathbf{h}_{\mathbf{k}}|\tau).
\end{aligned} \tag{A4}$$

These equations show the relations between the angles $(\varphi_{\mathbf{k}}, \theta_{\mathbf{k}})$ and the dynamics of spin polarization. In the following, we show that these relations can used to determine $(\varphi_{\mathbf{k}}, \theta_{\mathbf{k}})$ through three spectroscopic sequences (I, II, and III), as shown in Fig. 4(c) in the main text. In all sequences, atoms are initially prepared in the state $|g\rangle$ at half filling without SOC.

In sequence I, a π pulse along σ_x is applied using the clock laser to induce the $|g\rangle \to |e\rangle$ transition at the same quasimomentum. Such a π pulse can be implemented using one of the four SOC beams, with the other three turned off by electro-optic amplitude modulators. We can selectively excite atoms at certain $\mathbf{k}^*$ using a weak pulse (compared to the tight-binding bandwidth), such that only atoms near $\mathbf{k}^*$ are excited to $|e\rangle$ and atoms away from $\mathbf{k}^*$ are off resonance and remain in state $|g\rangle$. Then we turn on the 2D (3D) SOC for an interval τ and let the system evolve under the Hamiltonian Eq. (2) in the main text. Even for a weak pulse, atoms near resonance momenta $\mathbf{k}^*$ may still be partially pumped to $|e\rangle$ (with amplitude $f_{\mathbf{k}}$). Because of the partial excitation amplitude $f_{\mathbf{k}}$, the spin polarization becomes a complex function of $\sqrt{1-|f_{\mathbf{k}}|^2}, -if_{\mathbf{k}}, \tau, \mathbf{k}$, which is $\langle\mathbf{S}(\mathbf{k})\rangle_{\mathrm{I}} = \mathbf{P}(\sqrt{1-|f_{\mathbf{k}}|^2}, -if_{\mathbf{k}}, \tau, \mathbf{k})$.

To eliminate the effects of partial excitation, we introduce sequence II, which is the same as I except that the π pulse is along $-\sigma_x$, leading to the spin polarization $\langle\mathbf{S}(\mathbf{k})\rangle_{\mathrm{II}} = \mathbf{P}(\sqrt{1-|f_{\mathbf{k}}|^2}, if_{\mathbf{k}}, \tau, \mathbf{k})$. The average between these two sequences gives a simple form of the spin polarization as

$$\begin{aligned}
&\tfrac{1}{2}[\langle\mathbf{S}(\mathbf{k})\rangle_{\mathrm{I}} + \langle\mathbf{S}(\mathbf{k})\rangle_{\mathrm{II}}] \\
&\quad = \tfrac{1}{2}[\mathbf{P}(\sqrt{1-|f_{\mathbf{k}}|^2}, -if_{\mathbf{k}}, \tau, \mathbf{k}) + \mathbf{P}(\sqrt{1-|f_{\mathbf{k}}|^2}, if_{\mathbf{k}}, \tau, \mathbf{k})] \\
&\quad = \left(\tfrac{1}{2} - |f_{\mathbf{k}}|^2\right)\mathbf{T}(\theta_{\mathbf{k}}, \varphi_{\mathbf{k}}, \tau).
\end{aligned} \tag{A5}$$

Here $\mathbf{T}$ is given as

$$\begin{aligned}
T_z(\theta_{\mathbf{k}}, \varphi_{\mathbf{k}}, \tau) &= \cos^2\theta_{\mathbf{k}} + \sin^2\theta_{\mathbf{k}}\cos(2|\mathbf{h}_{\mathbf{k}}|\tau), \\
T_y(\theta_{\mathbf{k}}, \varphi_{\mathbf{k}}, \tau) &= \cos\theta_{\mathbf{k}}\sin\theta_{\mathbf{k}}\sin\varphi_{\mathbf{k}} \\
&\quad - \Theta\sin[2|\mathbf{h}_{\mathbf{k}}|\tau + \arctan(-\cos\theta_{\mathbf{k}}\tan\varphi_{\mathbf{k}})],
\end{aligned}$$

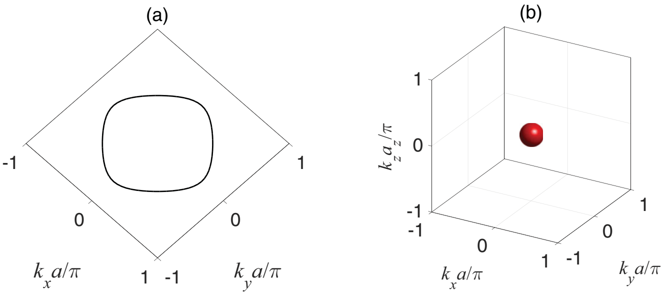

FIG. 5. The resonance momenta $\mathbf{k}^*$ induced by a narrow π pulse is a circle in two dimensions (a) and a spherical surface in three dimensions (b) which surrounds a Weyl point.

$$T_x(\theta_{\mathbf{k}}, \varphi_{\mathbf{k}}, \tau) = \cos\theta_{\mathbf{k}} \sin\theta_{\mathbf{k}} \cos\varphi_{\mathbf{k}} - \Gamma \sin\left[2|\mathbf{h}_{\mathbf{k}}|\tau + \arctan\left(\frac{\cos\theta_{\mathbf{k}}}{\tan\varphi_{\mathbf{k}}}\right)\right],$$

with $\Theta = \sqrt{(\cos\theta_{|\mathbf{k}|}\sin\theta_{|\mathbf{k}|}\sin\varphi_{|\mathbf{k}|})^2 + (\sin\theta_{|\mathbf{k}|}\cos\varphi_{|\mathbf{k}|})^2}$ and $\Gamma = \sqrt{(\cos\theta_{|\mathbf{k}|}\sin\theta_{|\mathbf{k}|}\cos\varphi_{|\mathbf{k}|})^2 + (\sin\theta_{|\mathbf{k}|}\sin\varphi_{|\mathbf{k}|})^2}$.

Finally, we use sequence III (which is the same as I without the π pulse) to filter the dynamics of the excited atoms from the remaining $|g\rangle$ atoms by canceling the 1/2 in Eq. (A5), yielding

$$\frac{\langle\mathbf{S}(\mathbf{k})\rangle_{\mathrm{I}} + \langle\mathbf{S}(\mathbf{k})\rangle_{\mathrm{II}}}{2} - \langle\mathbf{S}(\mathbf{k})\rangle_{\mathrm{III}} = |f_{\mathbf{k}}|^2\mathbf{T}(\theta_{\mathbf{k}}, \varphi_{\mathbf{k}}, \tau). \tag{A6}$$

Without the time-of-flight imaging, the experimentally measured spin polarization should be summed over the momentum space. We notice that $f_{\mathbf{k}}$ in Eq. (A6) is only nonzero around the $\mathbf{k}^*$ ring or surface (see Fig. 5). As a result, time-of-flight images are taken to determine the spin polarization $\langle\mathbf{S}\rangle$ at each $\mathbf{k}$ only on the $\mathbf{k}^*$ ring or surface, rather than the whole momentum space. That is to say, we use the time of flight to resolve the azimuthal direction of momentum, and the final observable for a certain point $\mathbf{k}^*$ is

$$\mathbf{O}(\mathbf{k}^*, \tau) = \int |f_{\mathbf{k}}|^2\mathbf{T}(\theta_{\mathbf{k}}, \varphi_{\mathbf{k}}, \tau)d|\mathbf{k}| \simeq c\mathbf{T}(\theta_{\mathbf{k}^*}, \varphi_{\mathbf{k}^*}, \tau). \tag{A7}$$

Here $c = \int |f_{\mathbf{k}}|^2 d|\mathbf{k}|$ is a constant (which is integrated in the radial direction) and we have taken into account that $f_{\mathbf{k}}$ is only nonzero around the $\mathbf{k}^*$. The angles $|\theta_{\mathbf{k}^*}|$ and $|\varphi_{\mathbf{k}^*}|$ can be inferred from the oscillations of $\mathbf{O}(\mathbf{k}^*, \tau)$:

$$\frac{O_z(\mathbf{k}^*, \tau)\mathrm{max} - O_z(\mathbf{k}^*, \tau)_{\mathrm{min}}}{2O_z(\mathbf{k}^*, \tau)\mathrm{mean}} = \tan^2\theta_{\mathbf{k}^*},$$

$$\frac{O_y(\mathbf{k}^*, \tau)\mathrm{max} - O_y(\mathbf{k}^*, \tau)_{\mathrm{min}}}{2O_y(\mathbf{k}^*, \tau)\mathrm{mean}} = \sqrt{1 + \frac{1}{\cos^2\theta_{\mathbf{k}^*}\tan^2\varphi_{\mathbf{k}^*}}},$$

$$\frac{O_x(\mathbf{k}^*, \tau)\mathrm{max} - O_x(\mathbf{k}^*, \tau)_{\mathrm{min}}}{2O_x(\mathbf{k}^*, \tau)\mathrm{mean}} = \sqrt{1 + \frac{\tan^2\varphi_{\mathbf{k}^*}}{\sin^2\theta_{\mathbf{k}^*}}}. \tag{A8}$$

$\theta_{\mathbf{k}^*}$ and $\varphi_{\mathbf{k}^*}$ are determined using the principle of continuity in the momentum space, as shown in Fig. 6.

For 2D Rashba SOC, there are eight momentum subspaces with different principles [see Figs. 6(a) and 6(b)]: (i) when $k_x > 0$, $k_y > 0$, and $k_xa/\pi + k_ya/\pi > 1$, principles are $|\theta_{\mathbf{k}}| = \theta_{\mathbf{k}}$ and $|\varphi_{\mathbf{k}}| + \pi = \varphi_{\mathbf{k}}$; (ii) when $k_x > 0$, $k_y > 0$, and $k_xa/\pi + k_ya/\pi < 1$, principles are $-|\theta_{\mathbf{k}}| + \pi = \theta_{\mathbf{k}}$ and $|\varphi_{\mathbf{k}}| + \pi = \varphi_{\mathbf{k}}$; (iii) when $k_x < 0$, $k_y > 0$, and $k_xa/\pi + 1 > k_ya/\pi$, principles are $|\theta_{\mathbf{k}}| = \theta_{\mathbf{k}}$ and $-|\varphi_{\mathbf{k}}| + \pi = \varphi_{\mathbf{k}}$; (iv) when $k_x < 0$, $k_y > 0$, and $k_xa/\pi + 1 < k_ya/\pi$, principles are $-|\theta_{\mathbf{k}}| + \pi = \theta_{\mathbf{k}}$ and $-|\varphi_{\mathbf{k}}| + \pi = \varphi_{\mathbf{k}}$; (v) when $k_x < 0$, $k_y < 0$, and $k_xa/\pi + k_ya/\pi < -1$, principles are $|\theta_{\mathbf{k}}| = \theta_{\mathbf{k}}$ and $|\varphi_{\mathbf{k}}| = \varphi_{\mathbf{k}}$; (vi) when $k_x < 0$, $k_y < 0$, and $k_xa/\pi + k_ya/\pi > -1$, principles are $-|\theta_{\mathbf{k}}| + \pi = \theta_{\mathbf{k}}$ and $|\varphi_{\mathbf{k}}| = \varphi_{\mathbf{k}}$; (vii) when $k_x > 0$, $k_y < 0$, and $k_xa/\pi > k_ya/\pi - 1$, principles are $|\theta_{\mathbf{k}}| = \theta_{\mathbf{k}}$ and $-|\varphi_{\mathbf{k}}| + 2\pi = \varphi_{\mathbf{k}}$; (viii) when $k_x > 0$, $k_y < 0$, and $k_xa/\pi < k_ya/\pi - 1$, principles are $-|\theta_{\mathbf{k}}| + \pi = \theta_{\mathbf{k}}$ and $-|\varphi_{\mathbf{k}}| + 2\pi = \varphi_{\mathbf{k}}$.

For 3D Weyl SOC, there also are eight momentum subspaces with different principles [see Figs. 6(c) and 6(d)]: (i) when $k_x > 0$, $k_y > 0$, and $k_z > 0$, principles are $|\theta_{\mathbf{k}}| = \theta_{\mathbf{k}}$ and $|\varphi_{\mathbf{k}}| = \varphi_{\mathbf{k}}$; (ii) when $k_x < 0$, $k_y > 0$, and $k_z > 0$, principles are $|\theta_{\mathbf{k}}| = \theta_{\mathbf{k}}$ and $-|\varphi_{\mathbf{k}}| + \pi = \varphi_{\mathbf{k}}$; (iii) when $k_x < 0$, $k_y < 0$, and $k_z > 0$, principles are $|\theta_{\mathbf{k}}| = \theta_{\mathbf{k}}$ and $|\varphi_{\mathbf{k}}| + \pi = \varphi_{\mathbf{k}}$; (iv) when $k_x > 0$, $k_y < 0$, and $k_z > 0$, principles are $|\theta_{\mathbf{k}}| = \theta_{\mathbf{k}}$ and $-|\varphi_{\mathbf{k}}| + 2\pi = \varphi_{\mathbf{k}}$; (v) when $k_x > 0$, $k_y > 0$, and $k_z < 0$, principles are $-|\theta_{\mathbf{k}}| + \pi = \theta_{\mathbf{k}}$ and $|\varphi_{\mathbf{k}}| = \varphi_{\mathbf{k}}$; (vi) when $k_x < 0$, $k_y > 0$, and $k_z < 0$, principles are $-|\theta_{\mathbf{k}}| + \pi = \theta_{\mathbf{k}}$ and $-|\varphi_{\mathbf{k}}| + \pi = \varphi_{\mathbf{k}}$; (vii) when $k_x < 0$, $k_y < 0$, and $k_z < 0$, principles are $-|\theta_{\mathbf{k}}| + \pi = \theta_{\mathbf{k}}$ and $|\varphi_{\mathbf{k}}| + \pi = \varphi_{\mathbf{k}}$; (viii) when $k_x > 0$, $k_y < 0$, and $k_z < 0$, principles are $-|\theta_{\mathbf{k}}| + \pi = \theta_{\mathbf{k}}$ and $-|\varphi_{\mathbf{k}}| + 2\pi = \varphi_{\mathbf{k}}$. Changing the frequency of the π pulse, we can obtain $\theta_{\mathbf{k}}$ and $\phi_{\mathbf{k}}$ in the whole momentum space.

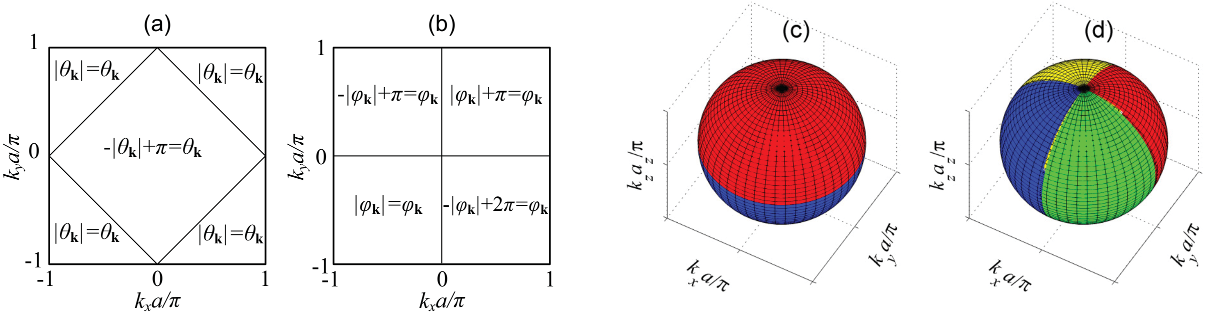

FIG. 6. (a, b) The relations between $|\theta_{\mathbf{k}}|$ and $\theta_{\mathbf{k}}$, and $|\varphi_{\mathbf{k}}|$ and $\varphi_{\mathbf{k}}$, in two dimensions. (c, d) The relations between $|\theta_{\mathbf{k}}|$ and $\theta_{\mathbf{k}}$, and $|\varphi_{\mathbf{k}}|$ and $\varphi_{\mathbf{k}}$, near +1 Weyl points in three dimensions. (c) In the red area $|\theta_{\mathbf{k}}| = \theta_{\mathbf{k}}$, and in the blue area $-|\theta_{\mathbf{k}}| + \pi = \theta_{\mathbf{k}}$. (d) In the red area $|\varphi_{\mathbf{k}}| = \varphi_{\mathbf{k}}$, in the yellow area $-|\varphi_{\mathbf{k}}| + \pi = \varphi_{\mathbf{k}}$, in the blue area $|\varphi_{\mathbf{k}}| + \pi = \varphi_{\mathbf{k}}$, and in the green area $-|\varphi_{\mathbf{k}}| + 2\pi = \varphi_{\mathbf{k}}$.

[1] D. Xiao, M.-C. Chang, and Q. Niu, Berry phases effects on electronic properties, Rev. Mod. Phys. **82**, 1959 (2010).

[2] M. Z. Hasan and C. L. Kane, Topological insulators, Rev. Mod. Phys. **82**, 3045 (2010).

[3] X.-L. Qi and S.-C. Zhang, Topological insulators and superconductors, Rev. Mod. Phys. **83**, 1057 (2011).

[4] J. E. Moore, The birth of topological insulators, Nature (London) **464**, 194 (2010).

[5] Y.-J. Lin, K. Jiménez-García, and I. B. Spielman, Spin-orbit-coupled Bose-Einstein condensates, Nature (London) **471**, 83 (2011).

[6] Z. Fu, P. Wang, S. Chai, L. Huang, and J. Zhang, Bose- Einstein condensate in a light-induced vector gauge potential using the 1064 nm optical dipole trap lasers, Phys. Rev. A **84**, 043609 (2011).

[7] J.-Y. Zhang, S.-C. Ji, Z. Chen, L. Zhang, Z.-D. Du, B. Yan, G.-S. Pan, B. Zhao, Y.-J. Deng, H. Zhai, S. Chen, and J.-W. Pan, Collective Dipole Oscillations of A Spin-Orbit Coupled Bose-Einstein Condensate, Phys. Rev. Lett. **109**, 115301 (2012).

[8] C. Qu, C. Hamner, M. Gong, C. Zhang, and P. Engels, Observation of Zitterbewegung in a spin-orbit coupled Bose-Einstein condensates, Phys. Rev. A **88**, 021604(R) (2013)

[9] A. J. Olson, S.-J. Wang, R. J. Niffenegger, C.-H. Li, C. H. Greene, and Y. P. Chen, Tunable Laudan-Zener transitions in a spin-orbit-coupled Bose-Einstein condensate, Phys. Rev. A **90**, 013616 (2014).

[10] P. Wang, Z. Yu, Z. Fu, J. Miao, L. Huang, S. Chai, H. Zhai, and J. Zhang, Spin-Orbit Coupled Degenerate Fermi Gases, Phys. Rev. Lett. **109**, 095301 (2012).

[11] L. W. Cheuk, A. T. Sommer, Z. Hadzibabic, T. Yefsah, W. S. Bakr, and M. W. Zwierlein, Spin-Injection Spectroscopy of a Spin-Orbit Coupled Fermi Gas, Phys. Rev. Lett. **109**, 095302 (2012).

[12] R. A. Williams, M. C. Beeler, L. J. LeBlanc, and I. B. Spielman, Raman-Induced Interactions in a Single-Component Fermi Gas Near an s-Wave Feshbach Resonance, Phys. Rev. Lett. **111**, 095301 (2013).

[13] L. Huang, Z. Meng, P. Wang, P. Peng, S.-L. Zhang, L. Chen, D. Li, Q. Zhou, and J. Zhang, Experimental realization of two-dimensional synthetic spin-orbit coupling in ultracold Fermi gases, Nat. Phys. **12**, 540 (2016).

[14] Z. Wu, L. Zhang, W. Sun, X.-T. Xu, B.-Z. Wang, S.-C. Ji, Y. Deng, S. Chen, X.-J. Liu, and J.-W. Pan, Realization of two-dimensional spin-orbit coupling for Bose-Einstein condensates, Science **354**, 83 (2016).

[15] Z. Meng, L. Huang, P. Peng, D. Li, L. Chen, Y. Xu, C. Zhang, P. Wang, and J. Zhang, Experimental Observation of a Topological Band Gap Opening in Ultracold Fermi Gases with Two-Dimensional Spin-Orbit Coupling, Phys. Rev. Lett. **117**, 235304 (2016).

[16] C. Nayak, S. H. Simon, A. Stern, M. Freedman, and S. D. Sarma, Non-Abelian anyons and topological quantum computation, Rev. Mod. Phys. **80**, 1083 (2008).

[17] F. Wilczek, Majorana returns, Nat. Phys. **5**, 614 (2009).

[18] C. Zhang, S. Tewari, R. M. Lutchyn, and S. Das Sarma, $p_x + ip_y$ Superfluid from s-Wave Interactions of Fermionic Cold Atoms, Phys. Rev. Lett. **101**, 160401 (2008).

[19] M. Gong, G. Chen, S. Jia, and C. Zhang, Searching for Majorana Fermions in 2D Spin-Orbit Coupled Fermi Superfluids at Finite Temperature, Phys. Rev. Lett. **109**, 105302 (2012).

[20] M. Gong, S. Tewari, and C. Zhang, BCS-BEC Crossover and Topological Phase Transition in 3D Spin-Orbit Coupled Degenerate Fermi Gases, Phys. Rev. Lett. **107**, 195303 (2011).

[21] Y. Xu, F. Zhang, and C. Zhang, Structured Weyl Points in Spin-Orbit Coupled Fermionic Superfluids, Phys. Rev. Lett. **115**, 265304 (2015).

[22] Y. Xu and L.-M. Duan, Type-II Weyl points in three-dimensional cold-atom optical lattices, Phys. Rev. A **94**, 053619 (2016).

[23] T. Dubček, C. J. Kennedy, L. Lu, W. Ketterle, M. Soljačić, and H. Buljan, Weyl Points in Three-Dimensional Optical Lattices: Synthetic Magnetic Monopoles in Momentum Space, Phys. Rev. Lett. **114**, 225301 (2015).

[24] B.-Z. Wang, Y.-H. Lu, W. Sun, S. Chen, Y. Deng, and X.-J. Liu, Dirac-, Rashba-, and Weyl type spin-orbit couplings: Toward experimental realization in ultracold atoms, Phys. Rev. A **97**, 011605 (2018).

[25] G. E. Volovik, *The Universe in a Helium Droplet* (Clarendon, Oxford, 2003).

[26] B. M. Anderson, I. B. Spielman, and G. Juzeliūnas, Magnetically Generated Spin-Orbit Coupling for Ultracold Atoms, Phys. Rev. Lett. **111**, 125301 (2013).

[27] Z. F. Xu, L. You, and M. Ueda, Atomic spin-orbit coupling synthesized with magnetic-field-gradient pulses, Phys. Rev. A **87**, 063634 (2013).

[28] Y. A. Bychkov and E. I. Rashba, Oscillatory effects and the magnetic susceptibility of carriers in inversion layers, J. Phys. C **17**, 6039 (1984).

[29] V. Galitski and I. B. Spielman, Spin-orbit coupling in quantum gases, Nature (London) **494**, 49 (2013).

[30] B. M. Anderson, G. Juzeliūnas, V. M. Galitski, and I. B. Spielman, Synthetic 3D Spin-Orbit Coupling, Phys. Rev. Lett. **108**, 235301 (2012).

[31] H. Zhai, Degenerate quantum gases with spin-orbit coupling: A review, Rep. Prog. Phys. **78**, 026001 (2015).

[32] X. Cui, B. Lian, T.-L. Ho, B. L. Lev, and H. Zhai, Synthetic gauge field with highly magnetic lanthanide atoms, Phys. Rev. A **88**, 011601 (2013).

[33] N. Q. Burdick, Y. Tang, and B. L. Lev, Long-Lived Spin-Orbit-Coupled Degenerate Dipolar Fermi Gas, Phys. Rev. X **6**, 031022 (2016).

[34] J. Dalibard, F. Gerbier, G. Juzeliunas, and P. Öhberg, Colloquium: Artificial gauge potentials for neutral atoms, Rev. Mod. Phys. **83**, 1523 (2011).

[35] M. L. Wall, A. P. Koller, S. Li, X. Zhang, N. R. Cooper, J. Ye, and A. M. Rey, Synthetic Spin-Orbit Coupling in an Optical Lattice Clock, Phys. Rev. Lett. **116**, 035301 (2016).

[36] L. F. Livi, G. Cappellini, M. Diem, L. Franchi, C. Clivati, M. Frittelli, F. Levi, D. Calonico, J. Catani, M. Inguscio, and L. Fallani, Synthetic Dimensions and Spin-Orbit Coupling with an Optical Clock Transition, Phys. Rev. Lett. **117**, 220401 (2016).

[37] S. Kolkowitz, S. L. Bromley, T. Bothwell, M. L. Wall, G. E. Marti, A. P. Koller, X. Zhang, A. M. Rey, and J. Ye, Spin-orbit-coupled fermions in an optical lattice clock, Nature (London) **542**, 66 (2017).

[38] S. L. Bromley, S. Kolkowitz, T. Bothwell, D. Kedar, A. Safavi-Naini, M. L. Wall, C. Salomon, A. M. Rey, and J. Ye, Dynamics of interacting fermions under spin-orbit coupling in an optical lattice clock, Nat. Phys. **14**, 399 (2018).

[39] T. Akatsuka, M. Takamoto, and H. Katori, Optical lattice clocks with non-interacting bosons and fermions, Nat. Phys. **4**, 954 (2008).

[40] T. Akatsuka, M. Takamoto, and H. Katori, Three-dimensional optical lattice clock with bosonic ^{88}Sr atoms, Phys. Rev. A **81**, 023402 (2010).

[41] N. D. Lemke, J. von Stecher, J. A. Sherman, A. M. Rey, C. W. Oates, and A. D. Ludlow, *p*-Wave Cold Collisions in an Optical Lattice Clock, Phys. Rev. Lett. **107**, 103902 (2011)

[42] S. L. Campbell, R. B. Hutson, G. E. Marti, A. Goban, N. Darkwah Oppong, R. L. McNally, L. Sonderhouse, J. M. Robinson, W. Zhang, B. J. Bloom, and J. Ye, A Fermi-degenerate three-dimensional optical lattice clock, Science **358**, 90 (2017).

[43] A. D. Ludlow, M. M. Boyd, J. Ye, E. Peik, and P. O. Schmidt, Optical atomic clocks, Rev. Mod. Phys. **87**, 637 (2015).

[44] A. A. Soluyanov, D. Gresch, Z. Wang, Q. Wu, M. Troyer, X. Dai, and B. A. Bernevig, Type-II Weyl semimetals, Nature (London) **527**, 495 (2015).

[45] M. Glück, A. R. Kolovsky, and H. J. Korsch, Wannier–Stark resonances in optical and semiconductor superlattices, Phys. Rep. **366**, 103 (2002).

[46] P. Lemonde and P. Wolf, Optical lattice clock with atoms confined in a shallow trap, Phys. Rev. A **72**, 033409 (2005).

[47] S. Blatt, J. W. Thomsen, G. K. Campbell, A. D. Ludlow, M. D. Swallows, M. J. Martin, M. M. Boyd, and J. Ye, Rabi spectroscopy and excitation inhomogeneity in a one-dimensional optical lattice clock, Phys. Rev. A **80**, 052703 (2009).

[48] L. Yi, S. Mejri, J. J. McFerran, Y. Le Coq, and S. Bize, Optical Lattice Trapping of ^{199}Hg and Determination of the Magic Wavelength for the Ultraviolet $^1S_0 \leftrightarrow {}^3P_0$ Clock Transition, Phys. Rev. Lett. **106**, 073005 (2011).

[49] P. G. Westergaard, J. Lodewyck, L. Lorini, A. Lecallier, E. A. Burt, M. Zawada, J. Millo, and P. Lemonde, Lattice-Induced Frequency Shifts in Sr Optical Lattice Clocks at the 10^{-17} Level, Phys. Rev. Lett. **106**, 210801 (2011).

[50] B. J. Bloom, T. L. Nicholson, J. R. Williams, S. L. Campbell, M. Bishof, X. Zhang, W. Zhang, S. L. Bromley, and J. Ye, An optical lattice clock with accuracy and stability at the 10^{-18} level, Nature (London) **506**, 71 (2014).

[51] K. W. Mahmud, L. Jiang, E. Tiesinga, and P. R. Johnson, Bloch oscillations and quench dynamics of interacting bosons in an optical lattice, Phys. Rev. A **89**, 023606 (2014).

[52] M. Greiner, O. Mandel, T. Esslinger, T. W. Hänsch, and I. Bloch, Quantum phase transition from a superfluid to a Mott insulator in a gas of ultracold atoms, Nature (London) **415**, 39 (2002).

[53] X.-J. Liu, K. T. Law, and T. K. Ng, Realization of 2D Spin-Orbit Interaction and Exotic Topological Orders in Cold Atoms, Phys. Rev. Lett. **112**, 086401 (2014).

[54] I. M. Lifshitz, Anomalies of electron characteristics of a metal in the high pressure region, Sov. Phys. JETP **11**, 1130 (1960).

[55] X. Wan, A. M. Turner, A. Vishwanath, and S. Y. Savrasov, Topological semimetal and Fermi-arc surface states in the electronic structure of pyrochlore iridates, Phys. Rev. B **83**, 205101 (2011).

[56] A. Yariv and P. Yeh, *Photonics: Optical Electronics in Modern Communications* (Oxford University, London, 2007).

[57] G.-B. Jo, J. Guzman, C. K. Thomas, P. Hosur, A. Vishwanath, and D. M. Stamper-Kurn, Ultracold Atoms in a Tunable Optical Kagome Lattice, Phys. Rev. Lett. **108**, 045305 (2012).

[58] T. H. Barter, T.-H. Leung, M. Okano, M. Block, N. Y. Yao, and D. M. Stamper-Kurn, Spatial coherence of a strongly interacting Bose gas in the trimerized Kagome lattice, arXiv:1906.11444 (2019).

[59] T. H. Barter, Ph.D. thesis, University of California, Berkeley, 2018.